PHYSICAL REVIEW B **106**, 155136 (2022)

Editors' Suggestion

Crystal electric field and properties of 4f magnetic moments at the surface of the rare-earth compound $TbRh_2Si_2$

Artem V. Tarasov,[1] Daria Glazkova,[1] Susanne Schulz,[2] Georg Poelchen,[2] Kristin Kliemt,[3]
Alexej Kraiker,[3] Matthias Muntwiler,[4] Clemens Laubschat,[2] Alexander Generalov,[5] Craig Polley,[5]
Cornelius Krellner,[3] Denis V. Vyalikh,[6,7] and Dmitry Yu. Usachov[1,*]
[1]St. Petersburg State University, 7/9 Universitetskaya nab., St. Petersburg, 199034, Russia
[2]Institut für Festkörper- und Materialphysik, Technische Universität Dresden, D-01062 Dresden, Germany
[3]Kristall- und Materiallabor, Physikalisches Institut, Goethe-Universität Frankfurt,
Max-von-Laue Strasse 1, D-60438 Frankfurt am Main, Germany
[4]Paul Scherrer Institut, Villigen, Switzerland
[5]Max IV Laboratory, Lund University, Box 118, 22100 Lund, Sweden
[6]Donostia International Physics Center (DIPC), 20018 Donostia/San Sebastián, Basque Country, Spain
[7]IKERBASQUE, Basque Foundation for Science, 48013, Bilbao, Spain

(Received 10 August 2022; accepted 4 October 2022; published 19 October 2022)

The crystal electric field (CEF) plays an essential role in defining the magnetic properties of 4f materials. It forces the charge density of 4f electrons and the related magnetic moment to be oriented along a certain direction in the crystal. The CEF and related magnetic properties were widely studied in the past with focus on bulk of 4f materials, while their surfaces have not received much attention. By the example of the antiferromagnetic material $TbRh_2Si_2$ and using first-principles calculations and classical 4f angle-resolved photoemission (PE) measurements, we show how the CEF and related magnetic properties, linked with the orientation of 4f moments, are modified at the surface region. Precisely, we studied the CEF characteristics in individual Tb layers for Tb- and Si-terminated surfaces of $TbRh_2Si_2$. We show how strongly the CEF changes near the surface and how dramatically it influences the orientation of the 4f moments relative to the bulk. The instructive message of our study is that a rather valuable information about the CEF-related phenomena can be derived from the temperature dependence of 4f PE spectra. The presented methodology including the theoretical approach can be further applied to many other layered and quasi-2D rare-earth-based materials for unveiling their surface magnetic properties.

DOI: 10.1103/PhysRevB.106.155136

I. INTRODUCTION

In the development of novel 4f-based systems for magnetic applications, including heterostructures and multilayers, it is essential to monitor and control the magnetic properties originating from individual atomic layers of lanthanides [1]. During the assembling of quasi-two-dimensional 4f objects, the magnetic properties, which are associated with the orientation of the 4f magnetic moments, can be dramatically modified due to the changes of the crystal electric field (CEF) near the interfaces [2]. The CEF influences the orientation of 4f magnetic moments, which in turn defines the orientation of the appeared magnetic exchange fields [3]. Therefore, it is necessary to elaborate the methodology, which would include theoretical approach and experimental expertise, allowing to control the properties linked with the CEF and orientation of the 4f magnetic moments in the individual atomic layers.

Much efforts have been directed towards studying the CEF and unveiling the related magnetic properties in the bulk of rare-earth-based materials. CEF can be studied experimentally using such methods as inelastic neutron scattering [4–6], resonant inelastic soft x-ray scattering [7–9], x-ray absorption spectroscopy [5,10–12], etc. However, all these techniques are rather bulk-sensitive and do not provide information about CEF at the surface or interfaces. One way to overcome this limitation is to study thin films, where the number of bulk atoms is comparable with the number of surface or interface atoms, as it was recently demonstrated using Raman spectroscopy [13]. Alternatively, *ab initio* calculations can be used to study CEF in individual atomic layers. However, reliable evaluation of crystal field parameters (CFPs) from the first principles remains challenging. It is known that usually calculations based on density functional theory (DFT) fail to describe correctly the fine electronic structure and CFPs for 4f materials due to the problems of self-interaction, strong correlation effects, and mixing of localized 4f states with the itinerant valence states [14–16]. Therefore, CEF calculations often rely on the experimental determination of splitting of the 4f states. As a result, CEF calculations are usually performed for the bulk [2,14,17,18], while theoretical studies of CEF at the surfaces or interfaces remain few in number [19–22].

In general, it is natural to expect that CEF at the surface or interface may strongly differ from that in the bulk [23] since

---

[*] dmitry.usachov@spbu.ru

the breaking of translational symmetry together with possible reconstructions and relaxations in the near-surface region may cause strong changes in charge distribution. This idea already finds confirmations both in experiment [13] and theory [19]. Here, we present a combined experimental and theoretical approach to study CEF in the individual rare-earth layers near the crystal surface. Performing theoretical investigations, we met with the known difficulties of applying DFT-based calculations to the $4f$ materials. However, our studies show that the results of ARPES measurements of the $4f$ multiplets and their further analysis with DFT-based calculations become rather useful for understanding how the CEF-dependent properties of the $4f$ states change near the crystal surface. The main aim of our paper is to elaborate a methodology, which can be applied to layered $4f$-based systems allowing to derive the CFPs and determine the orientation of magnetic $4f$ moments governed by CEF in individual atomic layers near the surface. We employ the extremely high surface sensitivity of photoelectron spectroscopy and utilize the strong dependence of the photoemission matrix element on the ground-state properties [24]. We also demonstrate to which extent the DFT calculations can be useful in describing the CEFs for the individual rare-earth layers.

As a model system, we consider the well-known antiferromagnetic (AFM) compound $\mathrm{TbRh_2Si_2}$, which has a Néel temperature T_N of 94 K and belongs to the remarkable family of layered $RET_2\mathrm{Si}_2$ materials, where RE and T denote a rare-earth element and a transition metal atom, respectively [25]. Its AFM phase is characterized by ferromagnetic (FM) order in the ab planes with out-of-plane orientation of the Tb $4f$ moments. The neighboring Tb planes, separated by Si–Rh–Si trilayers, are AFM-coupled to each other along the c axis.

Due to much weaker chemical bonds between Tb and Si atomic layers, as compared to the tightly bound Si–Rh–Si blocks, the crystals of $\mathrm{TbRh_2Si_2}$ cleave predominantly perpendicular to the c axis between Tb and Si atomic layers, uncovering either terbium- or silicon-terminated surface [25]. This gives us an opportunity to perform comparative studies of how the CEF and related properties are changed in individual Tb layers near both Tb and Si surfaces by means of theory and experiment.

II. METHODS

Growth of $\mathrm{TbRh_2Si_2}$ single crystals was carried out according to the method described in Ref. [26]. Samples were cleaved *in situ* under ultrahigh vacuum (UHV) conditions at low temperature. PED measurements were performed at the X03DA (PEARL) beamline [27] of the Swiss Light Source using a Scienta EW4000 electron analyzer. ARPES data were obtained at the BLOCH beamline of the MAX IV synchrotron radiation facility equipped with a Scienta DA30 analyzer. Linear polarization of photons was used. The normal to the sample surface, the x-ray beam, the polarization vector of photons, and the axis of the analyzer lens were oriented in the horizontal plane, while the entrance slit was oriented vertically. PED maps were measured by rotating the sample with a polar angle step of 1° and azimuthal angle step of 20°, while the acceptance angle of the analyzer was about ±25°. The 2D electron detector allowed mapping of the angular distribution with an azimuthal angle step of less than 0.5°.

Calculations of one-electron PE matrix elements including PED were performed using the EDAC code [28]. Uncertainties were estimated in accordance with Ref. [29]

First-principles calculations of CEF in the framework of the density functional theory (DFT) were performed in the Computing Center of SPbU Research Park. Here we use the augmented plane waves + local orbital method implemented in the WIEN2k program [30]. For the exchange correlation functional the generalized-gradient approximation form [31] was adopted. For the calculations the experimental lattice parameters of $\mathrm{TbRh_2Si_2}$ [32] were used, while the atomic positions within the unit cell were relaxed until the forces on each atom were less than 1 mRy/a_0, where a_0 is a Bohr radius. The distance between the neighboring Tb ions was 4.04 Å. The atomic sphere radii were set to 2.50 a_0 for Tb, 2.48 a_0 for Rh, and 1.83 a_0 for Si. The $4f$ orbitals located on neighboring Tb sites have nonzero overlap, which makes the interpretation of results less transparent. To reduce this overlap, we used a (2×2) lateral supercell. The near-surface region was modeled by a periodic slab, consisting of six four-layer $\mathrm{TbRh_2Si_2}$ blocks and terminated by Tb and Si atoms on both sides and a vacuum region, which extends over 15 Å. The eigenvalue problem was solved in a k-point grid of $6 \times 6 \times 12$ of the irreducible Brillouin zone of the bulk cell and $6 \times 6 \times 1$ for the surface one. The parameter determining the accuracy of the calculations within the APW + lo method, $RMT \times K_{\max}$ was set to 5.5, where RMT is the smallest atomic sphere radius and $K_{\max}$ is the plane wave basis set cutoff. The self-consistent field (SCF) calculations were performed without spin polarization and the $4f$ electrons were treated as core electrons, which contribute to the spherical component of the density only. After the standard self-consistent solution of the Kohn-Sham equations, we performed a non-SCF calculation with the Tb $4f$ states treated as valence states and then transformed the Bloch states from the $4f$ energy window to Wannier functions with the use of the wien2wannier interface [33] followed by standard application of the wannier90 software [34]. Wannier90 provides the local $4f$ Hamiltonian as a 7×7 matrix, which is then expanded in the matrix elements of spherical tensor operators. The expansion coefficients are the CEF parameters. Further details of the method are given in Ref. [14].

For calculations of photoemission intensity, structural optimization of the model 32-layer slab was done using the full potential (FP) local-orbital minimum-basis method implemented in the FPLO-14.00-48 code (improved version of the original FPLO code by Koepernik and Eschrig [35]) with the use of local density approximation (LDA) and open-core (OC) approximation [25].

III. RESULTS AND DISCUSSION

A. Angle-resolved photoemission from the 4*f* shell and the 4*f* Hamiltonian

In order to model PE spectra from an open $4f$ shell, we treat f electrons as core states neglecting their interaction with valence states, which is of minor importance in the case of

Tb compounds. We work in the basis of LS-coupled states $|wLSJM_J\rangle$, where w is a set of quantum numbers, which distinguishes different states with identical quantum numbers LSJ. The matrix element for electric dipole transitions from the initial state $|wLSJM_J\rangle$ to the final state $|w'L'S'J'M'_J,\vec{k}m_s\rangle$, which is an antisymmetrized product of the states of ion $|w'L'S'J'M'_J\rangle$ and photoelectron $|\vec{k}m_s\rangle$, may be written as [36]

$$\left\langle w'L'S'J'M'_J,\vec{k}m_s \mid \vec{\varepsilon}\cdot\sum_{i=1}^{N}\vec{r}_i \mid wLSJM_J\right\rangle = \sqrt{N}Q^{w'L'S'}_{wLS}\sum_m U^{L'S'J'M'_Jmm_s}_{LSJM_J}D_m(\vec{k}), \tag{1}$$

where $\vec{\varepsilon}$ is the photon polarization vector, while N is the occupation number of the 4f shell. The factor $Q^{w'L'S'}_{wLS}$ is the fractional parentage coefficient, and D_m is the one-electron matrix element of dipole transition from the atomic 4f-orbital $|mm_s\rangle$ to the continuum state $|\vec{k}m_s\rangle$. The factor U involves four Clebsch-Gordan coefficients [36]

$$U^{L'S'J'M'_Jmm_s}_{LSJM_J} = \sum_{\substack{MM_S\\M'M'_S}} C^{LM}_{L'M'\,lm}\,C^{SM_S}_{S'M'_S\,\frac{1}{2}m_s}\,C^{JM_J}_{LM\,SM_S}\,C^{J'M'_J}_{L'M'\,S'M'_S}, \tag{2}$$

where $l = 3$ for the f shell. By means of standard algebraic manipulations [37], we obtain

$$U^{L'S'J'M'_Jmm_s}_{LSJM_J} = \Pi_{JJ'LS}(-1)^{J+M'_J+\frac{1}{2}}\sum_{k(\varkappa)}(-1)^{k+\frac{1}{2}}C^{k\varkappa}_{lm\,\frac{1}{2}m_s} \times C^{k\varkappa}_{J'-M'_J\,JM_J}\begin{Bmatrix} L & S & J\\ L' & S' & J'\\ l & \frac{1}{2} & k\end{Bmatrix}, \tag{3}$$

where we used a notation $\Pi_{ab\ldots} = \sqrt{(2a+1)(2b+1)\cdots}$. The summation index in brackets means that the respective sum contains only one term.

As a first step, we consider a Hamiltonian of an isolated ion with Coulomb, spin-orbit and configuration interactions, using the same methodology as in Ref. [38]. Spin-orbit interaction leads to intermediate coupling by mixing different LS states, while J and M_J remain good quantum numbers. Thus, the eigenstates are considered as the following linear combinations:

$$|JM_J\rangle = \sum_{wLS} C^J_{wLS}\,|wLSJM_J\rangle. \tag{4}$$

By diagonalizing the Hamiltonian matrix, we obtain the energies and coefficients C^J_{wLS} and $C^{J'}_{w'L'S'}$ for the f^N and f^{N-1} configurations before and after photoionization, respectively. The parameters of the Hamiltonian can be found in Ref. [39].

When the atom is influenced by CEF and/or magnetic field, J and M_J cease to be good quantum numbers. However, in view of the large 4f multiplet splittings of RE ions it is a common practice and a good approximation to consider only one J term with the lowest energy, which is possibly split in $2J+1$ levels. Thus, for the initial state of the ion we truncate the basis to a set of $|M_J\rangle$ states. In this case, the eigenstates are formed as the following linear combinations:

$$|\nu\rangle = \sum_{M_J} A^{\nu}_{M_J}\,|M_J\rangle = \sum_{wLSM_J} A^{\nu}_{M_J}C^J_{wLS}\,|wLSJM_J\rangle,$$

where ν is the state number. The eigenvectors A^{ν} can be obtained by diagonalizing the CEF Hamiltonian with possible magnetic interactions [Eq. (9)]. In photoemission, CEF and magnetic splitting in the final state are usually not resolved, therefore, they can be neglected. Then, for the PE cross section of transition between the initial state $|\nu\rangle$ and the final states $|J'M'_J,\vec{k}m_s\rangle$ with all possible M'_J and m_s we obtain

$$\sigma_{J'\nu}(\vec{k}) = \sum_{m_sM'_J}\left|\sum_{m(M_J)} A^{\nu}_{M_J}I^{mm_s}_{M_JJ'M'_J}D_m(\vec{k})\right|^2, \tag{5}$$

where we defined

$$I^{mm_s}_{M_JJ'M'_J} = \sqrt{N}\sum_{\substack{wLS\\w'L'S'}} C^J_{wLS}C^{J'}_{w'L'S'}Q^{w'L'S'}_{wLS}\,U^{L'S'J'M'_Jmm_s}_{LSJM_J}. \tag{6}$$

In the particular case when the influence of CEF can be neglected and the moment of the RE ion $\langle\vec{J}\rangle$ is oriented in Z direction, the 4f states are the $|M_J\rangle$ states (all $A^{\nu}_{M_J}$ are zero except for one), then the Eq. (5) is simplified to

$$\sigma_{J'M_J}(\vec{k}) = \sum_{mm_s(M'_J)}\left(I^{mm_s}_{M_JJ'M'_J}\right)^2\sigma_m(\vec{k}), \tag{7}$$

where $\sigma_m(\vec{k}) \propto |D_m(\vec{k})|^2$ are one-electron differential PE cross sections and D_m are the respective matrix elements. We used Eq. (7) to calculate 4f PE spectra for all trivalent lanthanides in Ref. [39].

When multiple initial states participate in photoemission, the differential cross section will include temperature-dependent occupancies $u_\nu(T)$ as

$$\sigma_{J'}(\vec{k},T) = \sum_{\nu}u_\nu(T)\sigma_{J'\nu}(\vec{k}), \qquad u_\nu \propto \mathrm{e}^{\frac{-E_\nu}{k_BT}} \tag{8}$$

where k_B is the Boltzmann constant and the energy levels E_ν are obtained from the 4f Hamiltonian.

In order to describe the ground state of Tb ions in the simulations of PE spectra of TbRh$_2$Si$_2$, we considered the following single-ion 4f Hamiltonian with molecular field exchange interaction

$$H = H_{\mathrm{CEF}} - \frac{3k_BT^0_C(g_e-1)^2}{J(J+1)(g_J-1)^2}\vec{S}\cdot\langle\vec{S}\rangle, \tag{9}$$

where J is the ground-state total moment, g_e is the g factor of electron, g_J is the Landé factor, T^0_C is an exchange interaction parameter, which is roughly equal to the Néel temperature in the absence of CEF, $\vec{S}$ is the vector of spin momentum operators S_X, S_Y, S_Z, and $\langle\vec{S}\rangle$ is the vector of their thermally averaged expectation values. The Hamiltonian (9) must be diagonalized self-consistently. For this purpose we use an iterative procedure; we start from a given $\langle\vec{S}\rangle$ oriented in the low-symmetry direction, find the eigenstates and calculate the new $\langle\vec{S}\rangle$ from them. This procedure is repeated until convergence is reached. Performing this procedure for each temperature, we obtain the temperature dependence of the magnetic moment. The parameter T^0_C is adjusted to obtain the desired temperature of magnetic ordering (T_C).

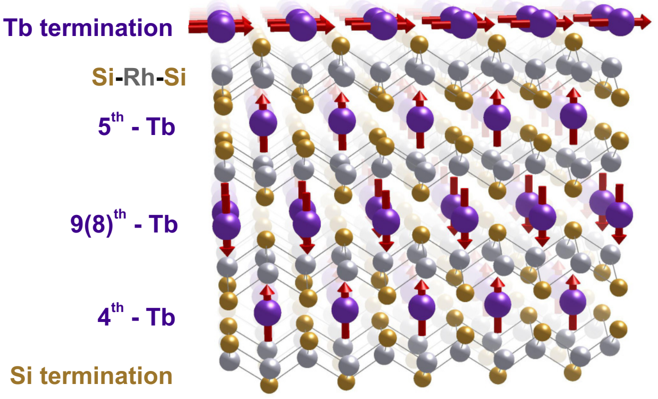

FIG. 1. Schematic view of the tetragonal AFM ordered $\mathrm{TbRh_2Si_2}$ crystal and its Tb and Si surfaces. The Tb atomic layers are well separated from each other by the tightly-bound Si-Rh-Si trilayer blocks. The $4f$ magnetic moments of Tb are shown by arrows. Reorientation of $4f$ moments at the Tb termination is caused by the changes of CEF at the surface (see discussion in text).

B. Photoemission spectroscopy analysis

Single crystals of $\mathrm{TbRh_2Si_2}$ cleave predominantly between the Tb and Si atomic layers, resulting in two possible surface terminations, which are shown schematically in Fig. 1. For the Tb-terminated surface presented in the upper part, we will refer to the surface Tb layer as well as the next subsurface Tb layer as first and fifth Tb layers, respectively. For the Si-terminated surface presented in the lower part, the two Tb layers closest to the surface are referred to as fourth and eighth Tb layers. The cleaved surface of $\mathrm{TbRh_2Si_2}$ usually demonstrates a coexistence of Si- and Tb-terminated terraces, which fortunately are usually larger than the spot size of the synchrotron radiation [39] and can be readily identified in ARPES measurements due to their remarkably different photoemission spectra.

Let us start by considering PE from $\mathrm{TbRh_2Si_2}$ at low temperature when the crystal is in the AFM phase. Figures 2(a) and 2(b) show ARPES maps of Tb- and Si-terminated surfaces, respectively. The Si termination can be easily identified due to characteristic surface states (SS), which exist around the $\overline{\mathrm{M}}$ points, as well as a cone-like surface resonance (SR), which is seen near the $\overline{\Gamma}$ point [25]. These bands are absent in the case of Tb termination. Besides dispersing valence bands, nondispersing $4f$ states of Tb are visible in the binding energy (BE) range of $3-12$ eV. These states appear due to transition from the ground $4f^8$ to the excited $4f^7$ configuration of Tb ion. Although the $4f^7$ configuration exhibits 327 $wLSJ$ states, which produce a Tb $4f$ multiplet, only a few of them give notable PE intensity.

Figure 2(c) demonstrates the PE spectra obtained from the $\overline{\Gamma}$ point region. One can see a striking difference in the lineshape of Tb $4f$ multiplet taken from the Si- and from the Tb-terminated surfaces. Particularly, the ^8S state situated at ~3 eV BE exhibits a high intensity in the spectrum taken from the Tb-terminated surface. However, it can hardly be identified among the valence states in the spectrum from the Si termination. Similarly, the ^6P and ^6I states, which are intense in case of the Tb termination, show rather weak intensity at the Si surface. Moreover, the $4f$-derived spectral structure is apparently more complex in case of the Tb termination. This is due to the surface core-level shifts of the $4f$ emission, which are a well-known phenomenon for lanthanides [40]. As expected, the spectral features from the first Tb layer are found to be shifted to higher BEs relative to the spectrum from the fifth Tb layer below the Tb surface as well as from the fourth Tb layer below the Si termination. We illustrate this observation for the ^6H PE peaks by dashed lines in Fig. 2(c). This interpretation is further confirmed by the PED data and their analysis, which will be discussed below.

In order to explain the observed large differences in the intensity distributions of the $4f$ multiplet components in the spectra recorded from two distinct terminations, let us consider an isolated Tb ion placed in a magnetic field aligned

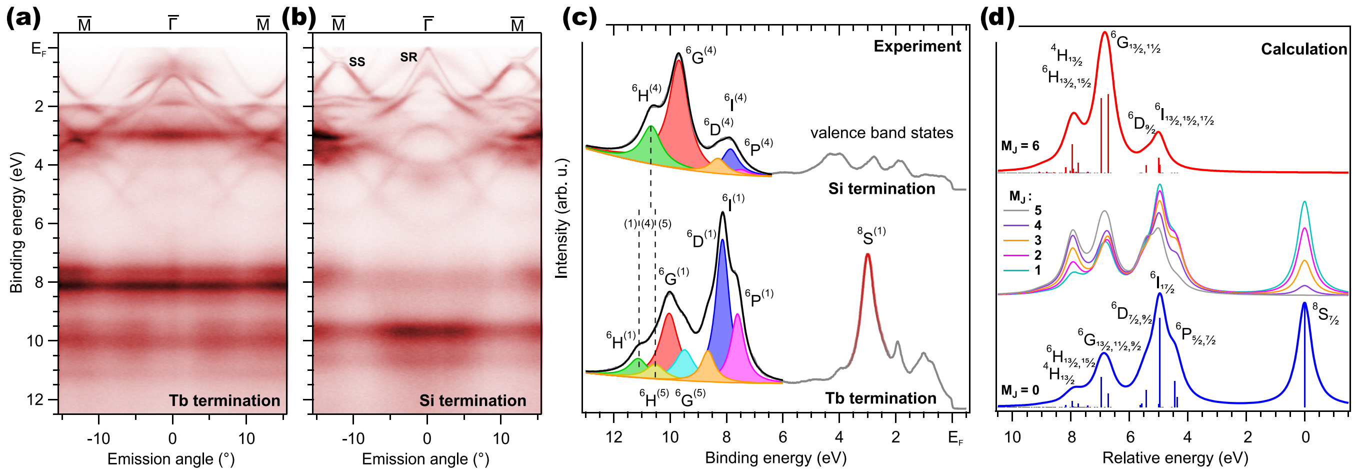

FIG. 2. ARPES spectra taken from (a) Tb and (b) Si terminated surfaces of the AFM ordered $\mathrm{TbRh_2Si_2}$ crystal at $T = 21$ K along the $\overline{\mathrm{M}}-\overline{\Gamma}-\overline{\mathrm{M}}$ direction of the surface Brillouin zone (SBZ). (c) Normal-emission PE spectra obtained by integration over the angle range of $\pm5^\circ$ from the data shown in [(a),(b)]. (d) Theoretical normal-emission $4f$ PE spectra for different single-M_J ground states calculated using Eq. (7). The numbers in brackets denote atomic layers from which the signal comes.

antiparallel to the Z axis. In this case, the ground state is described by $M_J = J = 6$. Then, for the Tb $^8S_{7/2}$ term, Eq. (7) is greatly simplified. The Clebsch-Gordan coefficients in Eq. (3) keep momentum projection conserved as $m + m_s = M_J - M'_J$. We further note that the $^8S_{7/2}$ peak corresponds to emission of one electron with m_s having opposite sign to the $M'_S = M'_J$ of the residual seven electrons of the 4f shell. This is only possible when $m_s = -1/2$, $M'_J = 7/2$ and $m = 3$. Thus, for the ^8S term $\sigma \propto \sigma_3$. The angular distribution of the σ_3 intensity is determined by the electric dipole selection rules $\Delta l = \pm 1$ and $\Delta m = 0, \pm 1$. For $l = m = 3$ the photoelectron wave function is composed of partial waves, which have angular parts described by spherical harmonics Y_2^2, Y_4^2, Y_4^3, and Y_4^4. All these functions take zero values for emission direction along the Z axis. This allows us to conclude that when the ground state of the Tb ion is described by $|M_J\rangle = |6\rangle$, there will be no ^8S emission along the direction of the Tb magnetic moment for any polarizations and energies of photons. The same is true for the magnetic state $|-6\rangle$ and PM state when the energy levels of the $|\pm 6\rangle$ states coincide.

Note that for the AFM ordered TbRh$_2$Si$_2$, the 4f magnetic moments of the Tb atoms lying in the fourth atomic layer below the Si surface [25] behave similarly to the bulk and have an out-of-plane orientation, i.e., parallel to the c axis. Thus, in this case a ground state close to $|6\rangle$ is rather expected that explains readily vanishing of the ^8S peak intensity. Then, a high intensity of the ^8S feature at Tb termination implies a strong canting of Tb 4f magnetic moments there. To verify this point, we calculated PE multiplet intensities for different $|M_J\rangle$ ground states of an isolated Tb ion using Eq. (7). In our calculations, we neglect PED effects, which, as we checked, have a minor influence on the lineshape of the 4f multiplet in our case. The obtained results are shown in Fig. 2(d) with vertical lines. The lengths of these lines are proportional to the intensities. For the most intense lines, the corresponding term symbols are given above. For comparison with experiment, we simulated PE spectra as sums of Lorentzians with a half width of 0.3 eV. It can be seen that a good agreement with experimental spectrum for Si termination is obtained at $|M_J| = 6$, while for Tb termination a good correspondence is achieved for $M_J = 0$. Summarizing the analysis of the 4f PE spectra presented above, we may conclude that magnetic moments of Tb experience strong reorientation at the Tb surface in comparison to those in the bulk. Namely, at the Tb surface, when it is magnetically ordered, they become oriented in-plane, while below the Si-terminated surface, the 4f moments have an out-of-plane orientation like in the bulk.

In order to understand how the magnetic ordering influences the lineshape of the 4f multiplet, we traced how the spectra change when the material undergoes the transition from the AFM to the PM phase. Our observations suggest that the normal-emission spectra remain almost unchanged. This result was expected since the magnetically ordered states $|6\rangle$, $|-6\rangle$ as well as the PM state with $|\pm 6\rangle$ doublet have identical theoretical normal-emission spectra when excitation with linearly polarized photons is considered. For the case when circular polarization is used, the spectra will be notably different. At this place, we should explicitly mention the importance of existence of magnetic domains. Namely, the Si-terminated surface always possesses magnetic domains, which reveal an opposite orientation of Tb 4f magnetic moments in the fourth Tb layer due to the steps of the Si-Rh-Si-Tb terraces. If these domains contribute on equal footing to the PE spectrum, then it is hardly possible to distinguish the difference between PM and magnetically ordered phases with any polarization of photons used. We expect, however, that with the use of spatially-resolved photoemission it should be possible to visualize the magnetic domains (to identify the regions with different orientations of the 4f moments) and to disclose the PM and FM phases based on the 4f PE spectra.

Note that magnetic ordering can also be detected by tracing the changes of the valence states. For the Si surface we can readily establish whether the Tb 4f moments are ordered below the Si-Rh-Si surface or not via observation of exchange splitting of the surface states [25]. Unfortunately, there are no such magnetically sensitive states at the Tb-surface. Therefore, it is not so straightforward to conclude whether the Tb surface is magnetically ordered or not. Our analysis of the 4f PE spectra recorded from the Tb termination only suggests that the states with M_J close to zero dominate in the ground state. Essentially, this is strikingly different from the bulk properties and from the case of a Si-terminated crystal. We suggest that the main reason of that are strong changes of crystal-electric field at the surface, which force reorientation of the Tb 4f moments. To verify and further explore this assumption, we performed theoretical calculations of CEF for different Tb layers.

C. CEF calculations

The TbRh$_2$Si$_2$ crystal has a D_{4h} symmetry in the bulk and a C_{4v} symmetry at the surface. For both cases the CEF Hamiltonian takes the following form:

$$H_{\mathrm{CEF}} = B_0^2 C_0^{(2)} + B_0^4 C_0^{(4)} + B_4^4\left(C_4^{(4)} + C_{-4}^{(4)}\right) + B_0^6 C_0^{(6)} + B_4^6\left(C_4^{(6)} + C_{-4}^{(6)}\right), \tag{10}$$

where B_q^k are CFPs and $C_q^{(k)}$ are spherical tensor operators.

The first attempt to study CEF in the bulk of TbRh$_2$Si$_2$ was made in Ref. [41] by determining only the B_0^2 parameter from the magnetic susceptibility analysis. Later on, the bulk CFP with notably smaller B_0^2 were estimated in Ref. [42] based on the parameters for HoRh$_2$Si$_2$, obtained experimentally from the temperature-dependent measurements of heat capacity. In the more recent paper [43] it was shown that CFPs obtained in Ref. [42] hardly reproduce the temperature dependence of the magnetic susceptibility (χ) and new CFPs (B_0^2 and B_0^4) were obtained by fitting the theoretical χ curve to the experimental one. The values of CFPs are given in the bottom of Table I.

So far, all experimental methods applied for determining the CFPs were mostly bulk sensitive and derived information was discussed in connection with the bulk properties. For elucidation of the surface properties and in particular those related to magnetism, the information about CFPs can be obtained from theoretical calculations. In this paper, we determine the CFPs for the bulk and surface layers of TbRh$_2$Si$_2$ by means of DFT calculations according to the procedure described in Ref. [14]. In spite of the fact that this method is best suited for insulators, it was also successfully applied

TABLE I. Crystal electric field parameters B_q^k in meV for sequence of the surface-related Tb atomic layers calculated within DFT, and bulk CEF parameters taken from literature as well as the values of molecular field parameter T_C^0 (K) obtained for each set of CFPs.

	Tb layer	B_0^2	B_0^4	B_4^4	B_0^6	B_4^6	T_C^0
DFT-nh	1	−108	−43.7	25.8	−9.7	23.0	69
	4	57.8	−38.7	20.0	−17.0	26.3	42
	5	0.8	−30.1	21.2	−14.8	25.1	95
	8 or 9	11.7	−31.5	21.7	−15.3	24.9	74
	bulk	11.5	−35.7	20.4	−14.8	20.1	74
DFT + Si $3p$	1	−87.9	−64.9	64.7	1.73	7.3	70
	4	74.9	−50.4	57.0	−16.4	19.0	39
	5	20.5	−43.7	61.3	−14.4	17.8	67
	8 or 9	30.3	−43.9	59.9	−15.9	18.6	56
	bulk	24.0	−49.1	45.1	−16.2	18.2	59
Best fit	bulk	36.83	−15.94				51
Literature	bulk [41]	41					50
	bulk [42]	18.60	−26.46	±5.75			64
	bulk [43]	40.95	−25.34				48

to metallic RE compounds [4]. In this procedure, a local $4f$ Hamiltonian, expressed in the basis of Wannier functions, is expanded in the matrix elements of spherical tensor operators. Wannier functions are obtained by transforming the Bloch functions calculated by means of DFT. The major problem in such approach is that DFT is not able to describe correctly the physics of strongly correlated systems (the $4f$ shell problem). In particular, hybridization between the $4f$ and valence states cannot be properly taken into account. This problem can be partially overcome by using the computational scheme proposed by Novák [14]. On the first step, the $4f$ electrons are treated as a spherically symmetric core shell to exclude the influence of their potential on CFPs. Afterwards, the charge density is kept fixed and the $4f$ orbitals are moved to the valence basis set where they may hybridize with the other valence states. However, this hybridization must be controlled manually by selecting which states may hybridize with the $4f$ states and by adjusting the energy position of the $4f$ orbitals relative to the valence states. Hence, this method contains an adjustable parameter Δ, which is the energy shift applied to the states. The case of the large energy separation between the valence and $4f$ states is the case of no hybridization (DFT-nh), when only the Kohn-Sham potential affects the CFPs. We will consider both cases with and without hybridization.

To determine which orbitals should be allowed to hybridize with the $4f$ states and to estimate the value of Δ, we used the CFPs obtained experimentally in Ref. [43] as a reference. By comparing the overall CEF splitting of the ground state in calculation and experiment, we have found that the best agreement is achieved when the $4f$ states are allowed to hybridize with the Si $3p$ states of neighboring atoms and when the latter are shifted by $\Delta = 0.18$ Ry above the $4f$ states. The obtained CFPs are given in Table I and the respective energy levels are shown in Fig. 3. It should be noted that the overall CEF splitting for CFPs calculated without hybridization is significantly lower than the experimental splitting in Ref. [43]. This indicates the importance of taking hybridization into account. The last column in Table I contains the exchange interaction parameters T_C^0 that we have chosen. From the temperature-dependent measurements of the exchange splitting of surface states at the Si-terminated surface we have found that the T_C for the fourth Tb layer is nearly equal to the T_N of the bulk, which is 94 K [44]. For the other layers, however, we do not know the T_C values, therefore we assumed that they all have a similar T_C equal to the bulk value. This assumption, indeed, does not affect our conclusions. Thus, all T_C^0 values in Table I were chosen to give the critical temperature equal to the T_N.

Using the model Hamiltonian [Eq. (9)] it is easy to find that the CEF parameter B_0^2 plays a decisive role in orientation of Tb $4f$ moments. Positive B_0^2 tends to align the moments out-of-plane, while negative B_0^2 leads to in-plane orientation. Which of the [100] and [110] in-plane directions will be preferred is determined mostly by the sign of the B_4^4 parameter. The CFPs calculated in this paper (with or without hybridization) lead to the orientation of the $4f$ moments along the [001] (out-of-plane) direction for the Si termination and along the [110] in-plane direction for the topmost Tb layer of the Tb termination. According to the calculation, in the magnetically ordered phase the ground state for the fourth Tb layer below the Si termination is nearly equal to the state $|6\rangle$ (or $|-6\rangle$), while for the first Tb layer of the Tb termination the ground state by 86% consists of states $|0\rangle$ and $|\pm 1\rangle$. Thus, the calculated signs of the B_0^2 parameters are in full agreement with the conclusions drawn from the PE intensity analysis.

To illustrate the influence of CEF on the orientation of the $4f$ magnetic moment, we present a visualization of the CEF potential, corresponding to the CFPs determined for the first and the fourth Tb layers for Tb and Si surfaces, respectively. Together with that, we also show the electron density distribution $|\rho_f|$ for the states $|0\rangle$ and $|6\rangle$. Figure 3(b) reveals the CEF potential $-V_{\text{CEF}}(R, \theta, \phi)$ (with negative sign) as a function of angles at the fixed distance R from the Tb site, corresponding to the maximum in the radial charge density distribution of the $4f$ orbitals. The energy of the $4f$ state is determined by the product of $\rho_f(\vec{r})$ and $V_{\text{CEF}}(\vec{r})$. The energy minimum is reached when the maximal density is located at the minimum of potential. This is fulfilled when ρ_f and $V_{\text{CEF}}^{\max} - V_{\text{CEF}}$ are most similar in their shapes. Hence, the CEF with maximum in Z direction favors the ground state $|0\rangle$ as it is shown in Fig. 3(b).

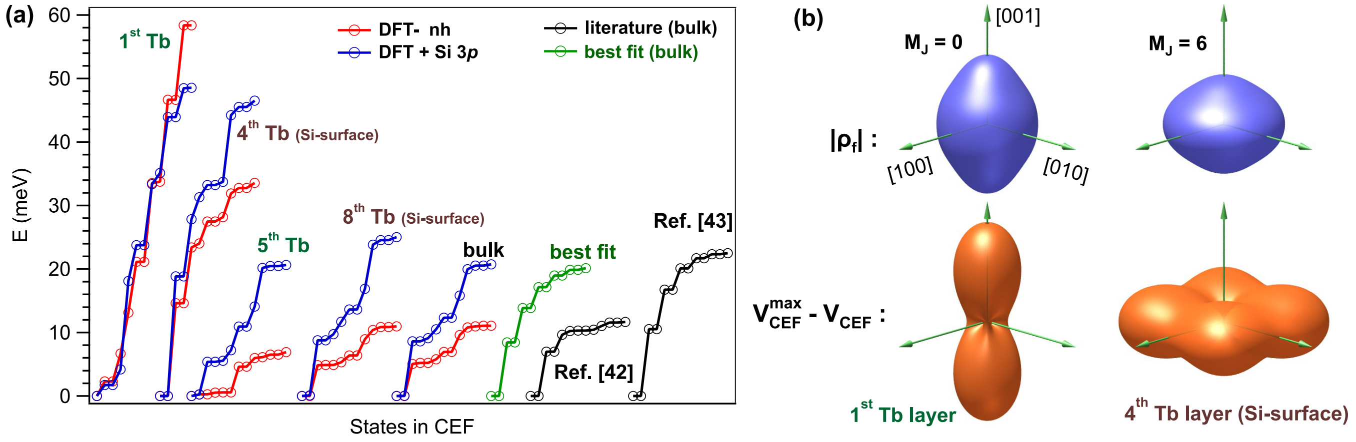

FIG. 3. (a) CEF energy levels calculated for different Tb atomic layers (1st and 5th for the Tb surface, and 4th and 8th for the Si surface.) The CEF states in respective sequences are shifted horizontally and connected with lines for better visual discrimination of degenerate and closely lying states. (b) The deviation of the CEF potential from its maximal value ($V_{\mathrm{CEF}}^{\max}(R) - V_{\mathrm{CEF}}(R,\theta,\phi)$) in real space for parameters determined for the 1st Tb layer (Tb surface) and for the 4th Tb layer (Si surface) along with the electron density distribution (ρ_f) for the states $|0\rangle$ and $|6\rangle$.

Another interesting result of the CEF calculation is a prediction that CEF in the fourth layer on the Si termination is notably larger than in the bulk, as it is evidenced by Fig. 3(a). As we will show in the next paragraph, this prediction can be confirmed experimentally with photoemission. It should be noted that we also performed CEF calculations with unrelaxed slabs and found that the surface structure relaxation does not influence the CFPs much. Hence, the opposite sign of the B_0^2 CFP for the first layer and the increased CEF splitting in the first and fourth layers are caused mainly by the crystal truncation.

D. Experimental analysis of CEF

Let us start with testing of the calculated bulk CFPs by comparing the theoretical temperature dependence of magnetic susceptibility χ with the experimental one. We calculated the magnetic susceptibility using LS coupling and the following 4f Hamiltonian with Heisenberg term for two sublattices:

$$H = \sum_{i=1}^{2} H_{\mathrm{CEF,i}} - \vec{\mu}_i \cdot \vec{B} - \frac{3k_B}{J(J+1)} \times \sum_{j=1}^{2} \left(T_{ij}^{a} J_{x,i}\langle J_{x,j}\rangle + T_{ij}^{a} J_{y,i}\langle J_{y,j}\rangle + T_{ij}^{c} J_{z,i}\langle J_{z,j}\rangle \right), \quad (11)$$

where $\vec{\mu}_i$ is a magnetic moment operator, $\vec{B}$ is an external magnetic field induction, T_{ij}^a and T_{ij}^c are molecular field parameters for the in-plane and out-of-plane directions, respectively. These parameters were fitted to obtain best agreement between theoretical and experimental dependencies $\chi(T)$.

Figure 4 shows the magnetic susceptibilities for single crystalline TbRh$_2$Si$_2$ along the [100] a axis (χ_a) and the [001] c axis (χ_c) of the crystal. The experimental data are compared with the theoretical temperature dependencies for different bulk CFPs. The CFPs from Ref. [43] were obtained by fitting of the theoretical curves to the experimental ones in the PM phase, hence, they provide good agreement above the T_N. However, they poorly reproduce the behavior of $\chi_a(T)$ in the AFM phase. By fitting in the whole range of temperatures, we determined the optimal parameters that nicely reproduce the experimental dependence in both PM and AFM phases. These CFPs are named as "best fit" in Table II. It was sufficient to use an isotropic model with $T_{ij}^a = T_{ij}^c$ to obtain good agreement with experiment. It should be noted that we used only the B_0^2 and B_0^4 CFPs since the other parameters have minor influence on susceptibility and cannot be determined uniquely. The susceptibility curves obtained for our DFT + Si 3p parameters do not give perfect agreement with experiment, indicating notable uncertainties in the calculated CFPs. This is not surprising, since the method that we used is known to be precise for insulators, but not for metals. Nevertheless, the qualitative predictions of the calculation agree well with our photoemission data. One of these predictions is a notably larger CEF in the fourth Tb layer on the Si termination

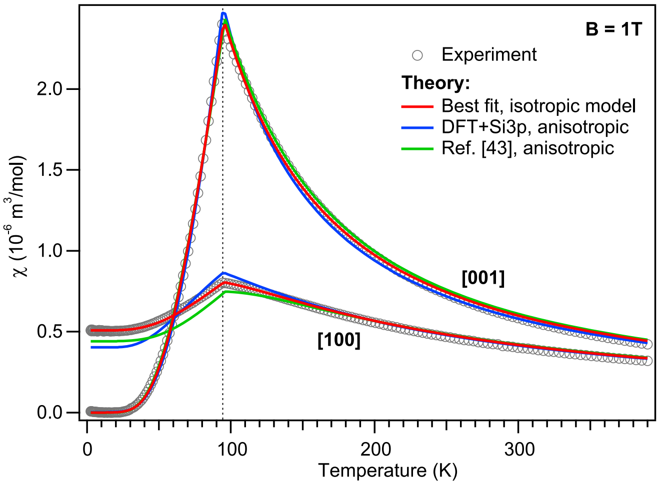

FIG. 4. Temperature dependencies of the magnetic susceptibility χ along the [001] and [100] crystallographic directions. Our experimental data are compared to the calculated χ for the CEF parameters given in Table I and molecular field parameters from Table II.

TABLE II. Optimized molecular field parameters.

CFP set	T_{11}^{a} (K)	T_{12}^{a} (K)	T_{11}^{c} (K)	T_{12}^{c} (K)
Ref. [43]	24.12	−24.34	17.93	−30.53
Best fit	20.27	−30.66	20.27	−30.66
DFT + Si $3p$	14.38	−44.66	29.47	−29.57

relative to the bulk. Let us discuss how this can be verified experimentally.

As it follows from Eq. (8), the $4f$ PE cross section includes temperature-dependent occupancies $u_\nu(T)$ of the energy levels split in CEF. Hence, the changes in the intensities of the multiplet components as a function of temperature are dependent on the CFPs of each near-surface RE layer contributing to the overall photoemission signal. This fact allows us to probe the energy splitting of the ground state by measuring the temperature dependence of the $4f$ PE spectra. To control the sensitivity of spectra to different atomic layers, we have to take into account the electron inelastic mean free path (IMFP) and the effect of PED. Note that both depend essentially on the kinetic energy of emitted photoelectrons. In this study, we have chosen two different photon energies of 110 eV and 200 eV. It is important that both energies are rather far from the Tb $4d \rightarrow 4f$ resonance at around 150 eV where the dipole matrix element is not valid.

Figure 5(a) presents the ARPES data taken from Si-terminated surface at $T = 195$ K and $h\nu = 200$ eV. Upon cooling down the intensities of the individual components of the $4f$ multiplet show different temperature dependencies. Figure 5(b) illustrates the changes in the intensity upon cooling down to 21 K. The respective angle-integrated spectra are presented in Fig. 5(c). The major changes are related to the $4f$ multiplet, while the intensity of the valence bands remains almost unchanged. Of course, the exchange splitting of the $\overline{\mathrm{M}}$ surface states emerges below the T_N [25], however it is not well-resolved on the large energy scale presented here. The difference plot allows us to unveil the temperature-dependent $4f$ spectral features. Namely, we were able to detect the presence of the ^8S peak, which is hardly visible in Fig. 5(a) due to its rather low intensity and strong overlap with the valence bands. The distorted shape of the ^8S peak in the angle-integrated difference spectrum may be a result of hybridization between the $4f$ states and the valence bands. This conclusion is further confirmed by the large width of the ^8S peak that is about 0.55 eV in contrast to the other multiplet components, which have the width of ~0.3 eV. This broadening becomes obvious upon comparison with theoretical spectra in Fig. 5(f), where we set the width of 0.3 eV for all multiplet components.

It is worth noting that for Fig. 5 we calculated the PE spectra as a sum of signals from three Tb layers in the model cluster. The interlayer distances in the cluster were taken from

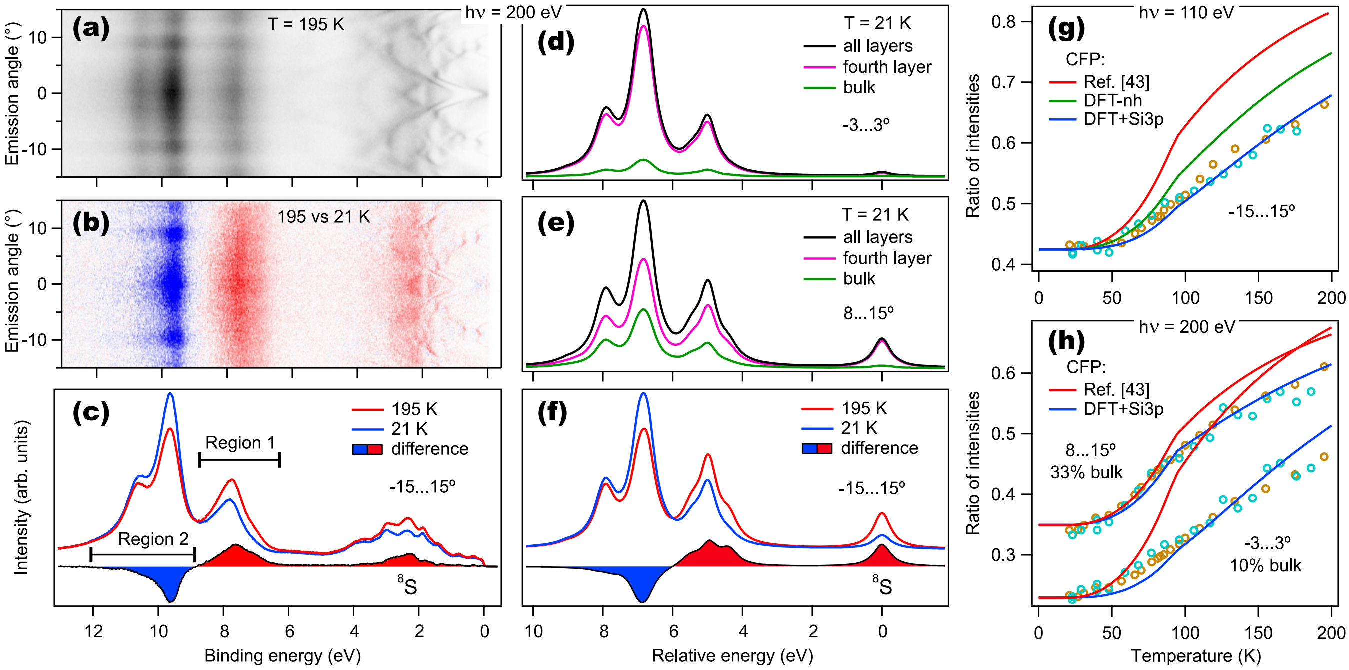

FIG. 5. (a) Experimental ARPES data taken in the $\overline{\mathrm{M}} - \overline{\Gamma} - \overline{\mathrm{M}}$ direction of the SBZ from the Si-terminated surface of $\mathrm{TbRh_2Si_2}$ at $T = 195$ K using $h\nu = 200$ eV. (b) Difference between the ARPES data measured at 195 K and 21 K. (c) The respective angle-integrated PE spectra and their difference. (d,e) Calculated PE spectra at 21 K integrated over the polar angle ranges of $0 \pm 3^\circ$ (d) and from 8 to 15° (e). The intensity from the fourth Tb layer is shown separately from the signal of deeper layers denoted as bulk. (f) Calculated angle-integrated PE spectra and their difference. The calculated spectra in [(d),(f)] were obtained with DFT + Si $3p$ CFPs. [(g),(h)] Measured temperature dependencies for the ratio of $4f$ PE intensities in the regions 1 and 2 shown in (c) are compared with the theoretical curves obtained for different CFPs. In the case of $h\nu = 110$ eV (g) the intensities were averaged over the angle range of $0 \pm 15^\circ$, while in the case of $h\nu = 200$ eV (h) we used two different angle regions: $0 \pm 3^\circ$ and from 8 to 15°. Two sets of experimental data shown by differently colored circles in (g) and (h) were obtained from two $\mathrm{TbRh_2Si_2}$ crystals.

a DFT calculation of surface relaxation [25]. For each Tb layer we computed the one-electron PE matrix elements $D_m(\vec{k})$ for their further use in Eq. (5). To describe the initial states, we selected the desired CFPs for each Tb layer. In Figs. 5(d), 5(e), and 5(f) we used the layer-dependent DFT + Si 3p CFPs. We took into account the AFM ordering of moments below the surface; however, it was assumed that the individual Tb layers have only in-plane exchange interactions and no interaction between different layers was considered. Hence, for each layer its own Hamiltonian Eq. (9) was diagonalized self-consistently. We also took into account the presence of magnetic domains. In particular, for the Si-terminated surface we assumed two possible orientations of magnetic moments along the c axis in the fourth and deeper Tb layers. For the case of $h\nu = 110\,\text{eV}$ we assumed the IMFP to be 5 Å, while for $h\nu = 200\,\text{eV}$ we used 7.5 Å.

Before analyzing the temperature dependencies, it is useful to estimate the surface sensitivity of PE spectra since it may notably depend on the emission angle due to PED. This is illustrated by Figs. 5(d) and 5(e), where the spectral intensities of the fourth layer and the other layers (bulk) are shown separately for two different emission angle ranges at $h\nu = 200\,\text{eV}$. The calculation predicts that upon transition from the normal emission ($0 \pm 3^\circ$) to the off-normal ($8 - 15^\circ$) geometry the contribution of the bulk layers to the multiplet intensity should rise from 10% to 33% in the energy range excluding the ^8S peak. Thus, by changing the PE angle in a rather small range one can vary the sensitivity of PE spectra to the selected atomic layers using PED effects. Thus, we have chosen the two aforementioned angle ranges for the further analysis of temperature dependence at $h\nu = 200\,\text{eV}$.

Figures 5(g) and 5(h) depict the temperature-dependent ratio of the 4f PE intensities of the two groups of multiplet components, which fall into the spectral ranges 1 and 2 shown in 5(c). The first region contains mainly the intensities of the lines ^6D, ^6I, and ^6P, while the second region includes the peaks ^6H and ^6G. The data were obtained from the Si-terminated surface only, since the Tb termination was too sensitive to contamination upon heating the sample. The data taken at $h\nu = 110\,\text{eV}$ were integrated in the angle range of $0 \pm 15^\circ$, while for $h\nu = 200\,\text{eV}$ we selected two angle ranges with different surface sensitivity. It should be noted that we applied correction factors of 1.05 and 0.9 to the calculated intensity ratios in the case of 110 eV and 200 eV photons, respectively, to achieve best agreement with experiment. This indicates that the relative uncertainty in our PE intensity calculations is about several percent.

In the modeling of the temperature-dependent PE spectra we used different CFPs from Table I. In the case of $h\nu = 110\,\text{eV}$, shown in Fig. 5(g), the bulk CFPs from Ref. [43] used for each Tb layer give a poor agreement with experiment. In this case, the model spectra show stronger temperature dependence than in the experiment. This means that the CEF-splitting of energy levels in the model is too small, therefore the excited levels are populated too rapidly with increasing temperature. Since the 4f PE signal mostly stems from the fourth layer, we may conclude that the CEF splitting there must be larger than in the bulk. One can see that the agreement between theory and experiment improves in the case of DFT-nh CFPs, for which the CEF splitting in the fourth layer is larger than in the bulk, as it is shown in Fig. 3. In the case of DFT + Si 3p CFPs the splitting becomes even larger and these parameters provide a very good agreement with experiment.

Rather similar results were obtained for the case of $h\nu = 200\,\text{eV}$, shown in Fig. 5(h). For the highly surface-sensitive angle range of $0 \pm 3^\circ$ the bulk CFPs from Ref. [43] give a bad agreement with experiment, while for the less surface-sensitive angle range from 8 to 15° the agreement is slightly better. This fact confirms that the bulk CFPs better describe the eighth layer rather than the fourth. The best agreement is again obtained with the DFT + Si 3p CFPs. Thus, we may conclude that (i) the CEF splitting in the fourth layer is notably larger than in the eighth layer or in the bulk and (ii) taking the Tb 4f−*Si* 3p hybridization into account in the CFP calculations improves agreement with the PE experiment.

The obtained results are instructive and demonstrate that classical 4f PE spectra contain a lot of information about the CEF-split 4f states. They allow to trace how the CEF changes at the subsurface and at the surface of rare-earth based materials and how orientation of 4f magnetic moments is affected by the modified CEF.

To make our study comprehensive, we decided to turn further to the PED experiments, which allow studying the structural properties of materials, surfaces and interfaces. For this purpose PE from closed core shells is usually applied. Our aim, however, will be to demonstrate that rich structural information can also be derived from analysis of intensity distributions of the individual 4f multiplet components. At the same time, we will verify the correctness of our PE calculations by comparing the simulated and measured PED patterns of the 4f multiplet components.

E. Photoelectron diffraction analysis

In order to explicitly confirm the assignment of different PE peaks in Fig. 2 to different atomic layers and test the validity of Eq. (5) for PE modeling, we analyzed the angular dependencies of 4f PE intensities (PED patterns). The necessity of sample rotation during PED measurements makes it challenging to obtain data from a single surface termination. The data presented in Fig. 6 were obtained from a mostly Tb-terminated crystal with small contribution of Si-terminated areas, which we neglect. Figure 6(e) shows the angle-integrated spectrum and its deconvolution in several components. The peak $^6G^{(1)}$, shown in Fig. 6(a), was modeled using Eqs. (8) and (5) as a signal from the 1st Tb layer in the PM state, using the eigenvectors A^{gr} of the Hamiltonian (10). Satisfactory agreement between calculated and measured $^6G^{(1)}$ PED patterns confirms our assignment of this PE peak to the 1st Tb layer. It is worth noting that assuming the ground state to be purely $|M_J\rangle = |0\rangle$, we obtained an almost identical theoretical PED pattern, indicating that this is a good approximation for PED analysis of the 1st Tb layer. Also, FM ordering of this layer in the calculation does not change the R factor much. However, when we calculated the PED pattern assuming no CEF and magnetic splitting of the ground state (in this case $\sigma \propto \sum_m \sigma_m$, similarly to the emission from a closed shell [45]) the main diffraction features remained,

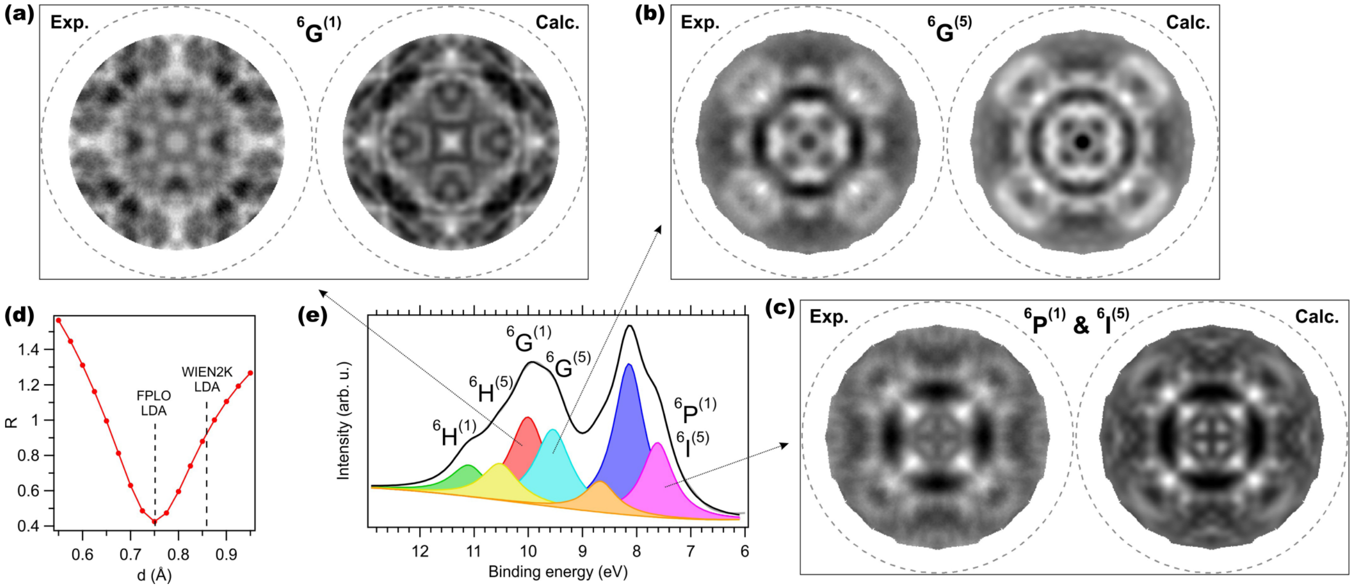

FIG. 6. [(a),(b),(c)] Experimental and calculated PED patterns in orthographic projection for several PE peaks shown in the spectrum (e). Dashed circles correspond to the emission angle of 90°. (d) R-factor dependence on the distance d between the Tb and Si atomic layers on the Tb-terminated surface. (e) Angle-integrated PE spectrum of Tb multiplet. The data were obtained from mostly Tb-terminated surface at $T \approx 30$ K and $h\nu = 110$ eV. In (b) and (c) the calculated patterns were smoothed to simulate experimental angle resolution of 1°.

but the R-factor increased by 36%. Thus, for PED analysis it is important to take CEF splitting of the ground state into account appropriately.

The neighbor peak $^6G^{(5)}$ demonstrates a very different PED pattern, shown in Fig. 6(b). Taking into account that the ground state in AFM phase is an almost pure state $|M_J\rangle = |6\rangle$ and populations of excited states are close to zero, we modeled this peak using Eq. (7). Good agreement with the experimental pattern suggests that this peak was correctly assigned to the 5th Tb layer. The peak with the lowest BE in Fig. 6(e) is formed by a superposition of the $^6P^{(1)}$ and $^6I^{(5)}$ PE signals from different Tb layers. We modeled the intensity of this peak by assuming the ground states to be $|0\rangle$ and $|6\rangle$ for the 1st and 5th Tb layers, respectively. The computed pattern exhibits a good agreement with experiment, indicating that such complex spectral structures as Tb $4f$ multiplet with surface BE shift can be used for PED analysis. As an example of such analysis we determine the relaxation value for the topmost atomic layer on the Tb terminated surface.

For structural analysis of Tb termination we used the $^6G^{(1)}$ PED pattern [Fig. 6(a)]. The relaxation value was optimized together with the inner potential and optimal values were found to be $d = 0.75 \pm 0.03$ Å and $V_0 = 16.5 \pm 2.5$. The R factor reached a value of 0.42, which is relatively large. Besides uncertainty of spectral deconvolution, the probable reason can be adsorption of residual gases, since the Tb surface is chemically extremely active even at low temperatures, while PED measurements are time-consuming. Nevertheless, the R-factor is very sensitive to the surface relaxation. Figure 6(d) demonstrates its dependence on the distance between the 1st Tb layer and 2nd Si layer. We have found that the distance where the R-factor minimum is reached perfectly matches the value of 0.75 Å predicted by DFT using the FPLO code with LDA and OC approximations. Considering that the calculated Tb-Si distance in the bulk crystal is 1.19 Å, the predicted relaxation is as large as 37%. This is rather unexpected because typical relaxation does not exceed 15%. It is worth noting that the LDA and OC calculation using the WIEN2k code gave a notably larger interlayer distance of 0.86 Å. Thus, DFT results are notably code-dependent in this case.

IV. CONCLUSIONS

We have studied CEF and related phenomena in the individual atomic layers of Tb near the Si- and Tb-terminated surfaces of the antiferromagnetic compound $TbRh_2Si_2$ by means of first-principles calculations based on DFT and $4f$ ARPES measurements. The latter give rich information about the $4f$ states and their properties through the analysis of the $4f$ multiplet spectral shape. Moreover, the temperature-dependent measurements of the $4f$ spectra allow estimating the energy splitting of the $4f$ states caused by CEF. Our results conclusively demonstrate that CEF and related magnetic phenomena at the surface of $4f$ materials are rather different from those in the bulk. We found that although the DFT-derived CFPs are not perfect for quantitative description of bulk magnetic properties, they give correct qualitative predictions about the changes of CEF in the near-surface region of $TbRh_2Si_2$. In particular, for the first atomic layer on Tb termination the DFT correctly predicts the inverted sign of the B_0^2 parameter. This inversion causes a canting of the Tb $4f$ moments by $\pi/2$ relative to their orientation in the bulk. Such canting manifests itself in strong changes of $4f$ PE spectra observed in the experiment. For Tb ions in the fourth atomic layer below the Si-terminated surface, the DFT predicts notably larger CEF splitting than that in the bulk. This prediction is fully confirmed by temperature-dependent PE measurements.

Finally, we have shown that PED patterns of individual components of the 4f multiplet can be used for structural analysis. In particular, we have determined the interlayer distance for Tb termination and found a giant inward relaxation of 37%, which is in agreement with the DFT calculation. This relaxation, however, is not responsible for the opposite sign of the B_0^2 CFP. The main reason of the modified CEF at the surface is related to the truncation of the crystal. Finally, we anticipate that strong modifications of CEF at the surfaces and subsurfaces may occur in many rare-earth based materials. Such modifications can dramatically change the magnetic properties in these regions and lead to novel temperature scales. We believe that the presented and tested methodology will greatly facilitate the control of magnetic exchange fields at surfaces and interfaces through magnetocrystalline anisotropy governed by CEF. Many compounds studied in the past can be re-examined using this method and many novel layered and quasi-2D *RE*-based systems, heterostructures, and nanostructures can be characterized on the respective subject.

ACKNOWLEDGMENTS

This work was supported by the Saint Petersburg State University (Grant No. 90383050). We acknowledge the German Research Foundation (DFG) through Grants No. KR3831/5-1, No. LA655/20-1, SFB1143 (Project No. 247310070), and TRR288 (No. 422213477, Project No. A03). D.V.V. acknowledges support from the Spanish Ministry of Science and Innovation, Project No. PID2020-116093RB-C44, funded by MCIN/AEI/10.13039/501100011033. We thank the Paul Scherrer Institut, Villigen, Switzerland for provision of synchrotron radiation beamtime at beamline PEARL of the SLS. We acknowledge MAX IV Laboratory for time on Beamline Bloch under Proposal No. 20190824 that was conducted in May and October of 2020. Research conducted at MAX IV, a Swedish national user facility, is supported by the Swedish Research Council under Contract No. 2018-07152, the Swedish Governmental Agency for Innovation Systems under Contract No. 2018-04969, and Formas under Contract No. 2019-0249.

---

[1] A. Hirohata, K. Yamada, Y. Nakatani, I.-L. Prejbeanu, B. Diény, P. Pirro, and B. Hillebrands, Review on spintronics: Principles and device applications, J. Magn. Magn. Mater. **509**, 166711 (2020).

[2] M. Kuz'min and A. Tishin, Chapter three theory of crystal-field effects in 3d-4f intermetallic compounds, in *Handbook of Magnetic Materials* Vol. 17, edited by K. Buschow (Elsevier, Amsterdam, Netherlands, 2007) pp. 149–233.

[3] B. G. Wybourne, *Spectroscopic Properties of Rare Earths* (Interscience Wiley, New York, 1965).

[4] Z. Huesges, K. Kliemt, C. Krellner, R. Sarkar, H.-H. Klauß, C. Geibel, M. Rotter, P. Novák, J. Kuneš, and O. Stockert, Analysis of the crystal electric field parameters of YbNi$_4$P$_2$, New J. Phys. **20**, 073021 (2018).

[5] T. Willers, D. T. Adroja, B. D. Rainford, Z. Hu, N. Hollmann, P. O. Körner, Y.-Y. Chin, D. Schmitz, H. H. Hsieh, H.-J. Lin, C. T. Chen, E. D. Bauer, J. L. Sarrao, K. J. McClellan, D. Byler, C. Geibel, F. Steglich, H. Aoki, P. Lejay, A. Tanaka *et al.*, Spectroscopic determination of crystal-field levels in CeRh$_2$Si$_2$ and CeRu$_2$Si$_2$ and of the 4f^0 contributions in CeM$_2$Si$_2$ (M=Cu, Ru, Rh, Pd, and Au), Phys. Rev. B **85**, 035117 (2012).

[6] M. Sundermann, K. Chen, H. Yavaş, H. Lee, Z. Fisk, M. W. Haverkort, L. H. Tjeng, and A. Severing, The quartet ground state in CeB$_6$: An inelastic x-ray scattering study, Europhys. Lett. **117**, 17003 (2017).

[7] A. Amorese, N. Caroca-Canales, S. Seiro, C. Krellner, G. Ghiringhelli, N. B. Brookes, D. V. Vyalikh, C. Geibel, and K. Kummer, Crystal electric field in CeRh$_2$Si$_2$ studied with high-resolution resonant inelastic soft x-ray scattering, Phys. Rev. B **97**, 245130 (2018).

[8] A. Amorese, G. Dellea, M. Fanciulli, S. Seiro, C. Geibel, C. Krellner, I. P. Makarova, L. Braicovich, G. Ghiringhelli, D. V. Vyalikh, N. B. Brookes, and K. Kummer, 4f excitations in Ce Kondo lattices studied by resonant inelastic x-ray scattering, Phys. Rev. B **93**, 165134 (2016).

[9] A. Amorese, K. Kummer, N. B. Brookes, O. Stockert, D. T. Adroja, A. M. Strydom, A. Sidorenko, H. Winkler, D. A. Zocco, A. Prokofiev, S. Paschen, M. W. Haverkort, L. H. Tjeng, and A. Severing, Determining the local low-energy excitations in the Kondo semimetal CeRu$_4$Sn$_6$ using resonant inelastic x-ray scattering, Phys. Rev. B **98**, 081116(R) (2018).

[10] P. Hansmann, A. Severing, Z. Hu, M. W. Haverkort, C. F. Chang, S. Klein, A. Tanaka, H. H. Hsieh, H.-J. Lin, C. T. Chen, B. Fåk, P. Lejay, and L. H. Tjeng, Determining the Crystal-Field Ground State in Rare Earth Heavy Fermion Materials Using Soft-X-Ray Absorption Spectroscopy, Phys. Rev. Lett. **100**, 066405 (2008).

[11] R. P. Amaral, R. L. Serrano, D. J. Garcia, D. Betancourth, P. G. Pagliuso, and J. G. Duque, Analysis of the crystal electric field ground state of intermetallic TbRhIn$_5$ by using soft x-ray absorption spectroscopy, in *Proc. 26th RAU: Ann. Users Meet. LNLS/CNPEM* (Sao Paulo, Brazil, 2016).

[12] F. Strigari, T. Willers, Y. Muro, K. Yutani, T. Takabatake, Z. Hu, Y.-Y. Chin, S. Agrestini, H.-J. Lin, C. T. Chen, A. Tanaka, M. W. Haverkort, L. H. Tjeng, and A. Severing, Crystal-field ground state of the orthorhombic Kondo insulator CeRu$_2$Al$_{10}$, Phys. Rev. B **86**, 081105(R) (2012).

[13] B. Halbig, U. Bass, J. Geurts, M. Zinner, and K. Fauth, Study of crystal-field splitting in ultrathin CePt$_5$ films by Raman spectroscopy, Phys. Rev. B **95**, 165115 (2017).

[14] P. Novák, K. Knížek, and J. Kuneš, Crystal field parameters with Wannier functions: Application to rare-earth aluminates, Phys. Rev. B **87**, 205139 (2013).

[15] P. Novák, K. Knížek, M. Maryško, Z. Jirák, and J. Kuneš, Crystal field and magnetism of Pr^{3+} and Nd^{3+} ions in orthorhombic perovskites, J. Phys.: Condens. Matter **25**, 446001 (2013).

[16] P. Novák, V. Nekvasil, and K. Knížek, Crystal field and magnetism with Wannier functions: Orthorhombic rare-earth manganites, J. Magn. Magn. Mater. **358-359**, 228 (2014).

[17] M. Richter, Band structure theory of magnetism in 3d-4f compounds, J. Phys. D: Appl. Phys. **31**, 1017 (1998).

[18] D. V. Shurtakova, P. O. Grishin, M. R. Gafurov, and G. V. Mamin, Using DFT to calculate the parameters of the crystal field in Mn^{2+} doped hydroxyapatite crystals, Crystals **11**, 1050 (2021).

[19] H. Moriya, H. Tsuchiura, and A. Sakuma, First principles calculation of crystal field parameter near surfaces of $Nd_2Fe_{14}B$, J. Appl. Phys. **105**, 07A740 (2009).

[20] Y. Toga, T. Suzuki, and A. Sakuma, Effects of trace elements on the crystal field parameters of Nd ions at the surface of $Nd_2Fe_{14}B$ grains, J. Appl. Phys. **117**, 223905 (2015).

[21] H. Tsuchiura, T. Yoshioka, and P. Novák, Bridging atomistic magnetism and coercivity in Nd-Fe-B magnets, Scr. Mater. **154**, 248 (2018).

[22] H. Tsuchiura, T. Yoshioka, P. Novák, J. Fischbacher, A. Kovacs, and T. Schrefl, First-principles calculations of magnetic properties for analysis of magnetization processes in rare-earth permanent magnets, Sci. Tech. Adv. Mater. **22**, 748 (2021).

[23] G. Poelchen, S. Schulz, M. Mende, M. Güttler, a. Generalov, A. V. Fedorov, N. Caroca-Canales, C. Geibel, K. Kliemt, C. Krellner *et al.*, Unexpected differences between surface and bulk spectroscopic and implied Kondo properties of heavy fermion $CeRh_2Si_2$, npj Quantum Mater. **5**, 70 (2020).

[24] G. van der Laan and B. T. Thole, Spin polarization and magnetic dichroism in photoemission from core and valence states in localized magnetic systems. II. Emission from open shells, Phys. Rev. B **48**, 210 (1993).

[25] D. Yu. Usachov, I. A. Nechaev, G. Poelchen, M. Güttler, E. E. Krasovskii, S. Schulz, A. Generalov, K. Kliemt, A. Kraiker, C. Krellner, K. Kummer, S. Danzenbächer, C. Laubschat, A. P. Weber, J. Sánchez-Barriga, E. V. Chulkov, A. F. Santander-Syro, T. Imai, K. Miyamoto, T. Okuda *et al.*, Cubic Rashba Effect in the Surface Spin Structure of Rare-Earth Ternary Materials, Phys. Rev. Lett. **124**, 237202 (2020).

[26] K. Kliemt, M. Peters, F. Feldmann, A. Kraiker, D.-M. Tran, S. Rongstock, J. Hellwig, S. Witt, M. Bolte, and C. Krellner, Crystal growth of materials with the $ThCr_2Si_2$ structure type, Cryst. Res. Technol. **55**, 1900116 (2020).

[27] M. Muntwiler, J. Zhang, R. Stania, F. Matsui, P. Oberta, U. Flechsig, L. Patthey, C. Quitmann, T. Glatzel, R. Widmer *et al.*, Surface science at the PEARL beamline of the Swiss Light Source, J. Synchrotron Radiat. **24**, 354 (2017).

[28] F. J. García de Abajo, M. A. Van Hove, and C. S. Fadley, Multiple scattering of electrons in solids and molecules: A cluster-model approach, Phys. Rev. B **63**, 075404 (2001).

[29] D. Yu. Usachov, A. V. Tarasov, K. A. Bokai, V. O. Shevelev, O. Y. Vilkov, A. E. Petukhov, A. G. Rybkin, I. I. Ogorodnikov, M. V. Kuznetsov, M. Muntwiler, F. Matsui, L. V. Yashina, C. Laubschat, and D. V. Vyalikh, Site- and spin-dependent coupling at the highly ordered *h*-BN/Co(0001) interface, Phys. Rev. B **98**, 195438 (2018).

[30] P. Blaha, K. Schwarz, F. Tran, R. Laskowski, G. K. H. Madsen, and L. D. Marks, WIEN2k: An APW+lo program for calculating the properties of solids, J. Chem. Phys. **152**, 074101 (2020).

[31] J. P. Perdew, K. Burke, and M. Ernzerhof, Generalized Gradient Approximation Made Simple, Phys. Rev. Lett. **77**, 3865 (1996).

[32] M. Ślaski, J. Leciejewicz, and A. SzytuŁa, Magnetic ordering in $HoRu_2Si_2$, $HoRh_2Si_2$, $TbRh_2Si_2$ and $TbIr_2Si_2$ by neutron diffraction, J. Magn. Magn. Mater. **39**, 268 (1983).

[33] J. Kuneš, R. Arita, P. Wissgott, A. Toschi, H. Ikeda, and K. Held, Wien2wannier: From linearized augmented plane waves to maximally localized Wannier functions, Comput. Phys. Commun. **181**, 1888 (2010).

[34] A. A. Mostofi, J. R. Yates, Y.-S. Lee, I. Souza, D. Vanderbilt, and N. Marzari, wannier90: A tool for obtaining maximally-localised Wannier functions, Comput. Phys. Commun. **178**, 685 (2008).

[35] K. Koepernik and H. Eschrig, Full-potential nonorthogonal local-orbital minimum-basis band-structure scheme, Phys. Rev. B **59**, 1743 (1999).

[36] A. P. Cox, *Fractional Parentage Methods for Ionisation of Open Shells of d and f Electrons. In Photoelectron Spectrometry. Structure and Bonding* (Springer, Berlin, 1975) pp. 59–81.

[37] D. Varshalovich, A. Moskalev, and V. Khersonskii, *Quantum Theory Of Angular Momemtum* (World Scientific Publishing, Singapore, 1988).

[38] F. Gerken, Calculated photoemission spectra of the $4f$ states in the rare-earth metals, J. Phys. F: Met. Phys. **13**, 703 (1983).

[39] D. Yu. Usachov, D. Glazkova, A. V. Tarasov, S. Schulz, G. Poelchen, K. A. Bokai, O. Yu. Vilkov, P. Dudin, K. Kummer, K. Kliemt, C. Krellner, and D. V. Vyalikh, Estimating the orientation of 4f magnetic moments by classical photoemission, J. Phys. Chem. Lett. **13**, 7861 (2022).

[40] M. Aldén, B. Johansson, and H. L. Skriver, Surface shift of the occupied and unoccupied 4f levels of the rare-earth metals, Phys. Rev. B **51**, 5386 (1995).

[41] B. Chevalier, J. Etourneau, J. Greedan, J. Coey, and A. Maaroufi, Single-crystal magnetic susceptibilities of $TbRh_2Si_2$. Determination of anisotropic exchange parameters, J. Less-Common Met. **111**, 171 (1985).

[42] Y. Takano, K. Ohhata, and K. Sekizawa, The low temperature magnetic anisotropy of the RRh_2Si_2 system (R: Rare earth elements), J. Magn. Magn. Mater. **70**, 242 (1987).

[43] H. Abe, H. Suzuki, and H. Kitazawa, High-field magnetization of single crystalline $TbRh_2Si_2$, J. Phys. Soc. Jpn. **71**, 1565 (2002).

[44] I. Felner and I. Nowik, Local and itinerant magnetism and superconductivity in RRh_2Si_2 (R = rare earth), Solid State Commun. **47**, 831 (1983).

[45] D. Yu. Usachov, A. V. Tarasov, S. Schulz, K. A. Bokai, I. I. Tupitsyn, G. Poelchen, S. Seiro, N. Caroca-Canales, K. Kliemt, M. Mende, K. Kummer, C. Krellner, M. Muntwiler, H. Li, C. Laubschat, C. Geibel, E. V. Chulkov, S. I. Fujimori, and D. V. Vyalikh, Photoelectron diffraction for probing valency and magnetism of $4f$-based materials: A view on valence-fluctuating $EuIr_2Si_2$, Phys. Rev. B **102**, 205102 (2020).